

Emergent Symmetry and Valley Chern Insulator in Twisted Double-Bilayer Graphene

Yimeng Wang,¹ G. William Burg,¹ Biao Lian,² Kenji Watanabe,³
Takashi Taniguchi,⁴ B. Andrei Bernevig,⁵ and Emanuel Tutuc^{1,*}

¹*Microelectronics Research Center, Department of Electrical and Computer Engineering,
The University of Texas at Austin, Austin, TX 78758, USA*

²*Princeton Center for Theoretical Science, Princeton University, Princeton, New Jersey 08544, USA*

³*Research Center for Functional Materials, National Institute of
Materials Science, 1-1 Namiki Tsukuba, Ibaraki 305-0044, Japan*

⁴*International Center for Materials Nanoarchitectonics,
National Institute of Materials Science, 1-1 Namiki Tsukuba, Ibaraki 305-0044, Japan*

⁵*Department of Physics, Princeton University, Princeton, New Jersey 08544, USA*

(Dated: December 2, 2024)

Theoretical calculations show that twisted double bilayer graphene (TDBG) under a transverse electric field develops a valley Chern number 2 at charge neutrality. Using thermodynamic and thermal activation measurements we report the experimental observation of a universal closing of the charge neutrality gap in the Hofstadter spectrum of TDBG at $1/2$ magnetic flux per unit cell, in agreement with theoretical predictions for a valley Chern number 2 gap. Our theoretical analysis of the experimental data shows that the interaction energy, while larger than the flat-band bandwidth in TDBG near 1° does not alter the emergent valley symmetry or the single-particle band topology.

Moiré patterns of two-dimensional (2D) materials provide a highly tunable platform for exploring correlated electronic states in electronic bands with flat dispersion. Celebrated examples include the twisted bilayer graphene (TBG) at the magic angle $\theta \simeq 1.1^\circ$ [1–5], twisted double-bilayer graphene [6–9], ABC trilayer graphene on hexagonal boron-nitride (hBN) [10, 11], twisted trilayer graphene [12–15], as well as fractional Chern insulators in twisted bilayer MoTe_2 [16–18] and pentalayer rhombohedral graphene on hBN [19], all of which exhibit superconducting or correlated insulator phases. Theoretical calculations show that a new emergent symmetry - which decouples two originally strongly intertwined valleys [1] - appears, and that, per each of the two valley emergent symmetry sectors, the electron bands of many moiré systems are topologically nontrivial. For example, TDBG and ABC trilayer graphene on hBN carry non-zero emergent-valley Chern numbers 2 and 3, respectively, under a transverse electric field [20–25]. Unlike correlated Chern insulators induced by interactions in the flat moiré bands, the valley Chern insulators in these systems stem from the nontrivial band topology protected by time-reversal invariance.

Experimental signatures of nontrivial band topology include transport experiments of the quantum spin Hall effect in 2D time-reversal invariant systems [26], the quantum anomalous Hall effect of Chern insulators in magnetic topological insulator thin films [27], and the angle-resolved photoemission spectroscopy and scanning tunneling microscope studies of 3D time-reversal invariant topological insulators [28–30]. In TDBG under transverse electric field the gap at charge neutrality carries a topological valley Chern number $C_V = 2$, protected by an emergent valley $U(1)$ symmetry [20–23, 25]. This emergent symmetry may be broken on the edge, leading

to back-scattering between the counter-propagating edge states from different valleys. Although interactions may drive moiré systems into a correlated Chern insulator with protected edge states [17–19, 31–34], such state is not necessarily related to the non-interacting band topology protected by the emergent valley symmetry. A bulk measurement of the band topological character per emergent symmetry sector (valley) is therefore necessary.

Theoretical studies suggest that the nontrivial band topology manifests itself in the Hofstadter butterfly, and can be observed through bulk magneto-transport [35–39]. In particular, a non-interacting band gap that carries a topological valley Chern number $C_V > 0$ is predicted to close at or before magnetic flux per unit cell $\Phi = (1/C_V)\Phi_0$ ($\Phi_0 = h/e$ is the flux quanta). Here, we present a combined experimental and theoretical study of magneto-transport in TDBG at $\theta = 0.97^\circ$, 1.01° and 1.33° . As a function of perpendicular magnetic field (B) the experimental data show an unexpected closing of the gap at charge neutrality when the flux per moiré unit cell $\Phi \approx (1/2)\Phi_0$ or smaller, in contrast with the tenets of the quantum Hall effect, which dictate that gaps increase as a function of B . This observation is consistent with the valley Chern number $C_V = 2$ of the valley-filtered flat bands, which supports both the band topology and the emergent symmetry that protects it. Furthermore, by theoretically analyzing the effect of interactions, we show that our experiment implies an interaction energy scale larger than the bandwidth of the flat bands in TDBG at $\theta = 1.01^\circ$, and that the interaction does not spoil the single-particle band topology and the emergent valley symmetry at charge neutrality.

Figure 1(a) shows a schematic of the TDBG sample, with hBN dielectrics and three gates – top, bottom, and substrate gates. The top and the bottom

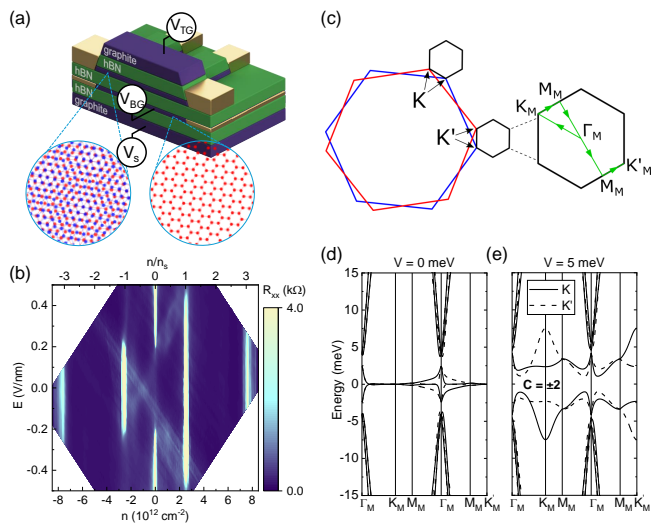


FIG. 1. (a) TDBG sample schematic with graphene top gate and graphene bottom gate. For chemical potential measurements the bottom gate is made of monolayer graphene and has multiple contacts. A substrate gate below the bottom gate is used to tune the E -field at which the chemical potential is measured. (b) Contour plot of R_{xx} vs. n and E measured in the TDBG sample with $\theta = 1.01^\circ$ at $T = 1.5$ K. The top axis shows n in units of n_s . (c) Decoupled moiré Brillouin zones arise at the K and K' points of the graphene bilayers. The enlarged view of the moiré Brillouin zone shows the high symmetry points and the path taken in momentum space for the (d-e) calculations. (d-e) Calculated moiré band structures at (d) $V = 0$ meV and (e) $V = 5$ meV. Solid (dashed) lines represent the moiré bands in the K (K') valleys of the graphene bilayers. At finite V , the gap at charge neutrality has Chern numbers $+2$ and -2 in the K and K' valleys, respectively.

gates are used to independently control the carrier density (n) and transverse electric field (E) in the TDBG. For the $\theta = 0.97^\circ$ sample the bottom gate, which is made of monolayer graphene and contacted with several electrodes, also acts as a resistively detected Kelvin probe to the TDBG chemical potential. The substrate gate is added to the dual gated geometry to tune the transverse E -field at which the TDBG chemical potential is measured [34].

Figure 1(b) shows the longitudinal resistance (R_{xx}) as a function of n and E in a TDBG sample with $\theta = 1.01^\circ$. The twist angle is defined such that in the limit $\theta = 0^\circ$ the TDBG approaches AB-AB stacking [Fig. 1(c)]. R_{xx} maxima along lines of constant n indicate energy gaps in the moiré band structure. The data show E -dependent, single particle gaps at charge neutrality ($n = 0$) and at fixed densities $\pm n_s$ and $\pm 3n_s$. Here, n_s is the carrier density required to fill a moiré unit cell with 4-fold spin-valley degeneracy, and is related to the twist angle by

$$n_s = 4 \frac{2}{\sqrt{3}} \left[\frac{\sin(\frac{\theta}{2})}{(a/2)} \right]^2;$$

$a = 2.46 \text{ \AA}$ is the graphene lattice constant. At charge neutrality, the band gap is initially small and increases with E , while the gaps at $\pm n_s$ decrease and eventually close at finite E . In addition, there are emerging R_{xx} maxima at $n = +\frac{1}{2}n_s$ within small windows of E around $\pm 0.3 \text{ V/nm}$, corresponding to developing correlated insulators at half-filling of the first conduction moiré band. Correlated insulators appear at half and quarter moiré band filling in TDBG flat bands as a result of strong electron-electron interaction [6–9, 40].

For small θ the TDBG moiré pattern reciprocal vector is much smaller than the intervalley momentum difference, which leads to distinct moiré Brillouin zones at the K and K' valleys of the parent graphene bilayers that are exponentially (in $1/\theta$) decoupled from one another [Fig. 1(c)]. This decoupling gives the moiré bands a valley degree of freedom, and an emergent valley U(1) rotation symmetry. Figures 1(d)-1(e) show $\theta = 1.01^\circ$ band structure calculations for zero and finite on-site energy difference (V) between neighboring graphene layers, respectively, and demonstrate the valley dependence of the bands. The V values are proportional to the applied transverse electric field E [41]. Furthermore, the calculated V -dependence is consistent with experimental observations, showing that the gap at charge neutrality opens with increasing E , and the gaps between the first and second moiré bands reduce or close.

At finite V , the gap that opens at charge neutrality is predicted to be topologically nontrivial [20–23, 25], with a valley-dependent Chern number of $C_K = +2$ or $C_{K'} = -2$ [Fig. 1(e)], which originates from the opening of two double Dirac cones of the same helicity in each valley. The gap thus carries a valley Chern number $C_V = (C_K - C_{K'})/2 = 2$ per spin, protected by the emergent valley U(1) symmetry, a bulk symmetry that can be broken by edge roughness. Instead, we explore here bulk signatures of the nonzero valley Chern number by examining the magneto-transport of TDBG in perpendicular magnetic fields, with an emphasis on the gap at charge neutrality. Figure 2(a) shows R_{xx} as a function of n and B for $E = 0.31 \text{ V/nm}$ in $\theta = 1.01^\circ$ TDBG. The combination of perpendicular magnetic fields and the spatial modulation of the moiré pattern leads to equally spaced Landau levels in the energy spectrum, and quantum Hall states (QHSs) when n and Φ satisfy the Streda formula [46, 47]:

$$\frac{n}{n_s} = \frac{\nu}{4} \frac{\Phi}{\Phi_0} + \sigma,$$

where $\Phi = BA_M$, $A_M = 4/n_s$ is the moiré unit cell area, and ν and σ are Landau level and moiré band filling factors, respectively. The best developed QHSs are labeled by their corresponding ν value in Fig. 2(a). An advantage of small twist angle TDBG is the large unit cell area, which makes high magnetic flux values relatively easy to access experimentally. As shown on the right axes of Fig.

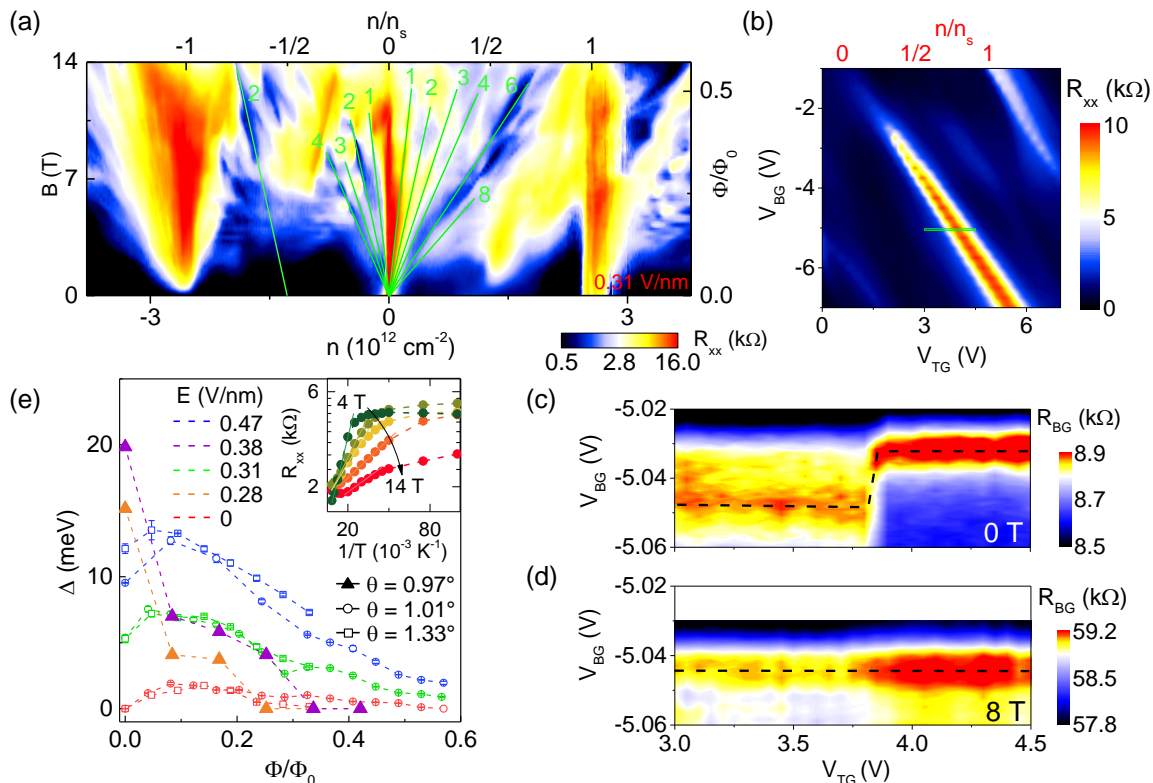


FIG. 2. (a) R_{xx} vs. n and B at $E = 0.31$ V/nm for TDBG with $\theta = 1.01^\circ$. The top axis shows n in units of n_s , and the right axis shows Φ/Φ_0 . The Landau level filling factor for well developed quantum Hall states are labeled. (b) R_{xx} vs. V_{TG} and V_{BG} for the $\theta = 0.97^\circ$ TDBG. The top axis shows n/n_s for the diagonal resistance maxima. (c-d) R_{BG} vs. V_{TG} and V_{BG} measured at (c) $B = 0$ T and (d) 8 T. Black dashed lines mark charge neutrality loci of the bottom gate graphene. Data are taken at $T = 1.5$ K in (a-d). (e) Δ vs. Φ/Φ_0 at different E -fields for three TDBG samples. The triangles represent thermodynamic measurements in the $\theta = 0.97^\circ$ TDBG; the circles and squares represent thermal activation measurements in the $\theta = 1.01^\circ$ and 1.33° TDBGs. Inset shows Arrhenius plot of R_{xx} vs. $1/T$ at charge neutrality for $E = 0.47$ V/nm, and at different B -fields for the $\theta = 1.01^\circ$ TDBG.

2(a), Φ/Φ_0 exceeds 1/2 at $B = 14$ T, values at which the predicted topological signatures should manifest.

Focusing now on the Φ/Φ_0 dependence of the gap at charge neutrality, Fig. 2(a) shows that R_{xx} at charge neutrality is initially large, and generally independent of B for low and moderate fields, but then decreases as Φ/Φ_0 approaches 1/2. While resistance is not necessarily a direct measure of an energy gap, especially when topological edge states may be present, these findings suggest that the gap at charge neutrality decreases at high magnetic flux in the vicinity of $\Phi/\Phi_0 = 1/2$. To substantiate this finding, a bulk measurement is needed. To that end, we measure the gap (Δ) at charge neutrality as a function of Φ/Φ_0 using a combination of thermodynamic measurements and thermal activation. Figure 2(b)-2(d) show the thermodynamic measurements in the $\theta = 0.97^\circ$ TDBG. In Fig. 2(b), R_{xx} as a function of V_{TG} and V_{BG} is shown, where the resistance maxima along the diagonal represent the TDBG charge neutrality. Figure 2(c) shows the resistance of the graphene bottom gate R_{BG} as a function of

V_{TG} and V_{BG} measured at $E = 0.38$ V/nm and $B = 0$ T. The R_{BG} is measured around the TDBG charge neutrality in the range marked by the green rectangle in Fig. 2(b), with the substrate gate at a fixed bias to shift the neutrality point of the bottom gate graphene to the target E -field. As detailed in Ref. [34], by tracing the charge neutrality of the bottom gate graphene, the chemical potential of the TDBG can be measured directly, revealing the bulk properties at charge neutrality. Specifically, the chemical potential of the TDBG can be calculated with $\mu = eV_{BG}(1 + C_s/C_{BG}) - eV_s C_s/C_{BG}$. Here, C_{BG} and C_s are the capacitance per unit area of the bottom and substrate gate dielectric, respectively, and V_s is the substrate gate bias. Accordingly, the change of μ is proportional to the change of V_{BG} when tracing the bottom gate charge neutrality plotted in Fig. 2(c), and the step the charge neutrality loci take at $V_{BG} \approx 3.8$ V reflects the TDBG thermodynamic gap at its charge neutrality, which is $\Delta = 20$ meV. The data for the same measurement at $B = 8$ T are shown in Fig. 2(d), where no gap

is observed. The values of Δ vs. Φ/Φ_0 measured in the $\theta = 0.97^\circ$ TDBG at fixed E -field values are shown in Fig. 2(e) (triangle symbols). Meanwhile, we perform thermal activation measurements on the $\theta = 1.01^\circ$ and 1.33° TDBGs [Fig. 2(e) inset], and summarize the thermodynamic and activation measurement results of Δ vs. Φ/Φ_0 in Fig. 2(e). Although differences exist between datasets, in both types of measurements the charge neutrality gap shows a closing behavior near or before $\Phi/\Phi_0 = 1/2$, which suggests a common origin of the gap closing. In the $\theta = 1.33^\circ$ TDBG, Δ shows a similar decreasing trend, but is only measurable up to $\Phi/\Phi_0 \simeq 0.3$ due to the larger twist angle.

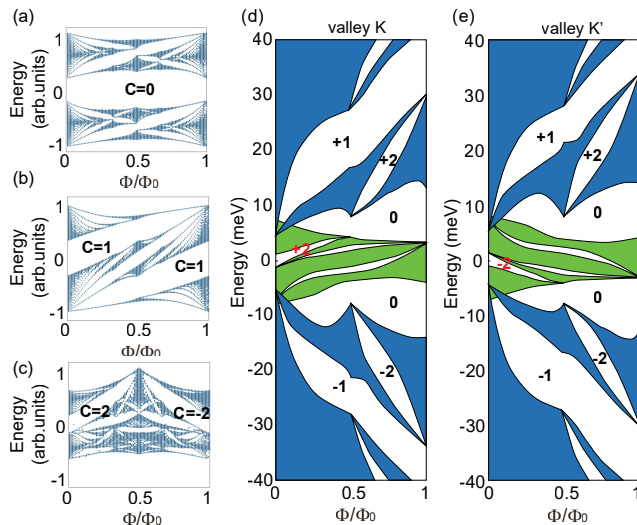


FIG. 3. (a-c) Hofstadter butterflies of 2-band Chern insulator tight-binding models with Chern numbers 0, 1 and 2, respectively. A gap of Chern number C is topologically protected to close at $\Phi/\Phi_0 = 1/C$. (d-e) The Hofstadter spectra of TDBG with $\theta = 1.01^\circ$ and $V = 5$ meV at valleys K and K' , respectively. The spectra include the lowest two moiré bands (green) and the higher moiré bands (blue). The integers label the Chern numbers of the dominant Hofstadter gaps.

The observations in Fig. 2 are surprising. For typical band-structures energy gaps are expected to open with increasing B . In magic angle TBG, a similar system with flat bands and strong interactions, compressibility measurements reveal the charge neutrality gap increases with B [48]. Consequently, as we explain below, the observed gap closing near $\Phi/\Phi_0 = 1/2$ is compelling evidence of the nontrivial topology of charge neutrality gap in TDBG, and of the emergent symmetry that protects the valley Chern number. It is important to distinguish between the valley Chern insulator in TDBG, and the correlated Chern insulators in TBG that break time reversal symmetry [49–51]. The fillings of the latter disperse in a perpendicular magnetic field according to the Streda formula [46, 47], similar to a quantum Hall state. The valley Chern gap in TDBG does not break

time reversal symmetry, and is not expected to disperse according to the Streda formula.

In the non-interacting band theory, the Hofstadter spectrum of a trivial band is usually bounded within its bandwidth, leaving the gap between topologically trivial bands open at any Φ/Φ_0 as shown in Fig. 3(a) [41]. In contrast, a topological gap will generically close at a certain magnetic flux, connecting the Hofstadter spectra above and below the gap. The simplest example is a Chern number C gap between two Chern bands of Chern numbers $\pm C$, which is topologically enforced to close at $\Phi/\Phi_0 = 1/|C|$ [35, 38, 39, 41]. Two examples of Chern number $C = 1$ and $C = 2$ gaps are shown in Fig. 3(b) and 3(c), respectively [41].

In TDBG with nonzero V , each valley has a Chern number ± 2 gap at charge neutrality, which is forced to close at $\Phi/\Phi_0 = 1/2$. Fig. 3(d)-3(e) show the Hofstadter butterflies at valley K and K' calculated [35, 38] using the non-interacting TDBG continuum model at $\theta = 1.01^\circ$ and $V = 5$ meV. The spectra of the lowest two moiré bands are shown in green. As expected, at $\Phi/\Phi_0 = 1/2$, the Chern number $C_K = 2$ ($C_{K'} = -2$) charge neutrality gap of valley K (K') closes at the top (bottom) of the lowest two moiré bands. Figure 4(a) shows the single valley gap with respect to Φ/Φ_0 at different V . This strongly suggests that the experimentally observed charge neutrality gap closing at $\Phi/\Phi_0 = 1/2$ in TDBG is due to the valley-dependent Chern number $C_K = -C_{K'} = 2$.

However, the midgap energies of the $C_K = 2$ and $C_{K'} = -2$ Chern gaps at valleys K and K' disperse oppositely with Φ , which differ by ~ 10 meV at $\Phi/\Phi_0 = 1/2$ [Fig. 3(d)-3(e)]. Furthermore, the Zeeman spin splitting is ~ 1 meV at $\Phi/\Phi_0 = 1/2$. Therefore, the total single-particle valley Chern gap of all spins and valleys at charge neutrality would close before $\Phi/\Phi_0 = 1/2$ due to energy band overlaps, as illustrated in Fig. 4(b). The calculated total valley Chern gap Δ of all spins and valleys for TDBG at $\theta = 1.01^\circ$ and different V closes no later than $\Phi/\Phi_0 \approx 0.2$ [Fig. 4(c)], and shows a gap re-opening around $0.2 < \Phi/\Phi_0 < 0.4$ due to other, further, Landau level gaps, different from our experimental observation. This discrepancy can be resolved by considering electron-electron interactions, which we treat here in a mean-field theory. Denote the band bottom and top of the first conduction (valence) moiré band at $\Phi = 0$ as M_1 ($-M_0$) and M_0 ($-M_1$), respectively, as shown in Fig. 4(b) ($M_0 > M_1 > 0$). For simplification, we assume the Chern gap of valley η ($+1$ for K and -1 for K') decreases linearly and closes at energy ηM_0 at $\Phi/\Phi_0 = 1/2$. The number of conduction (valence) states per area above (below) the gap at valley η and spin s is given by $N_{m,\eta}(\Phi) = (1 - 2m\eta\Phi/\Phi_0)/A_M$ ($m = \pm 1$ for conduction and valence bands, respectively).

We consider a local interaction particle-hole symmetric

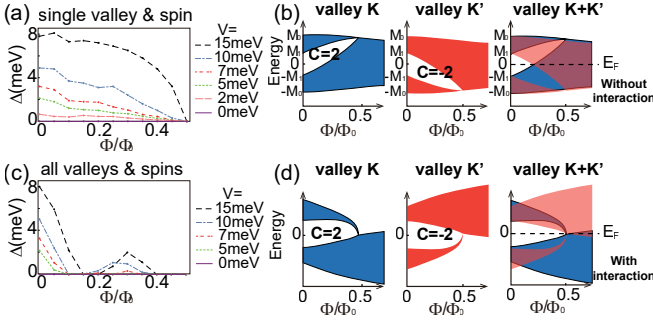


FIG. 4. (a) The $C_\eta = \pm 2$ Chern gap of a single valley and spin vs. Φ/Φ_0 . (b) Schematics of the non-interacting Hofstadter spectra at valley K and K' . The $C_\eta = \pm 2$ Chern gaps of the two valleys ($\eta = \pm 1$ for valleys K and K' , respectively) split in energy at finite magnetic field, leading to a total charge neutrality gap closing before $\Phi/\Phi_0 = 1/2$. (c) The total non-interacting charge neutrality gap of all spins and valleys of TDBG vs. Φ/Φ_0 , where spin g-factor 2 is used. (d) Illustration of the effective Hofstadter spectra under interaction by mean field theory, where the $C_\eta = \pm 2$ Chern gaps of valleys K and K' are enlarged and shifted towards each other, leading to a total charge neutrality gap closing around $\Phi/\Phi_0 = 0.5$.

about charge neutrality:

$$\mathcal{H}_I = \frac{U_0 A_M}{2} \sum_{m, m', \eta, \eta', s, s'} \gamma_{m\eta s}^{m' \eta' s'}(\Phi) \tilde{n}_{m, \eta, s} \tilde{n}_{m', \eta', s'},$$

where $U_0 > 0$ is the short-range interaction energy, $\tilde{n}_{m, \eta, s} = n_{m, \eta, s} - \frac{N_{m, \eta}(\Phi)}{2}$ is the electron density of indices $\{m, \eta, s\}$ relative to half-filling, with $0 \leq n_{m, \eta, s} \leq N_{m, \eta}(\Phi)$, and $\gamma_{m\eta s}^{m' \eta' s'}(\Phi) = 1 - \delta_{m, m'} \delta_{\eta, \eta'} \delta_{s, s'} - \delta_{m, -m'} \delta_{\eta, \eta'} \delta_{s, s'} \zeta(\Phi)$ accounts for reduced interaction within the same valley and spin due to Pauli exclusion [41]. We assume each band $\{m, \eta, s\}$ has a uniform density of states. This allows us to calculate the total mean-field energy at the filling of charge neutrality, and derive the ground-state charge neutrality gap $\Delta(\Phi)$ with respect to Φ [41]. We find two interaction effects: first, the charge neutrality gap at $\Phi = 0$ increases from the single-particle gap $2M_1$ to $\Delta(0) = 2M_1 + U_0$. Secondly, the charge-neutrality valley Chern gap $\Delta(\Phi)$ closes at $\Phi/\Phi_0 = \frac{2M_1 + U_0}{4M_0 + 4M_1 - 2U_0} < 1/2$ for weak interactions $0 < U_0 < M_0$ (but is larger than non-interacting cases), while the gap closes at $\Phi/\Phi_0 \approx 1/2$ for strong interactions $U_0 \geq M_0$, analogous to the single valley gap in Fig. 4(a). Heuristically, this is because the interaction increases the energy cost for a valence electron to jump into a conduction band, stabilizing the charge neutrality gap. In the mean field picture, the bands of the two valleys are effectively deformed by interaction as shown in Fig. 4(d), with their Chern gaps enlarged and shifted towards each other. Such a simplified mean field picture is further verified by our numerical Hartree-Fock calcula-

tion of the Hofstadter spectrum of a valley Chern number 2 tight-binding model with on-site Hubbard interactions [41].

Our experimental observations reveal the TDBG charge neutrality gap under a transverse E -field shows an unusual closing in the presence of a perpendicular magnetic field, consistent with a valley Chern insulator with $C_V = 2$. Moreover, the interaction energy U_0 , although larger than the flat band widths in TDBG near $\theta = 1^\circ$, preserves the emergent valley $U(1)$ symmetry and the valley Chern number. Our study provides a novel method to detect the band topology of 2D moirés and other superlattice systems by measurement of their bulk energy spectra.

The work at The University of Texas was supported by the National Science Foundation Grants MRSEC DMR-2308817 and EECS-2122476, Army Research Office under Grant No. W911NF-22-1-0160, and the Welch Foundation grant F-2169-20230405. Work was partly done at the Texas Nanofabrication Facility supported by NSF Grant No. NNCI-1542159. B.A.B. was supported by the Department of Energy Grant No. de-sc0016239, the Schmidt Fund for Innovative Research, Simons Investigator Grant No. 404513 the Packard Foundation. B.L. is supported by the National Science Foundation through Princeton University's Materials Research Science and Engineering Center DMR-2011750, and the National Science Foundation under award DMR-2141966. K.W. and T. T. acknowledge support from the Elemental Strategy Initiative conducted by the MEXT, Japan (Grant No. JPMXP0112101001) and JSPS KAKENHI (Grants No. JP19H05790 and No. JP20H00354).

* Corresponding Author: etutuc@mail.utexas.edu

- [1] R. Bistritzer and A. H. MacDonald, Proc. Natl. Acad. Sci. **108**, 12233 (2011).
- [2] Y. Cao, V. Fatemi, S. Fang, K. Watanabe, T. Taniguchi, E. Kaxiras, and P. Jarillo-Herrero, Nature **556**, 43 (2018).
- [3] Y. Cao, V. Fatemi, A. Demir, S. Fang, S. L. Tomarken, J. Y. Luo, J. D. Sanchez-Yamagishi, K. Watanabe, T. Taniguchi, E. Kaxiras, R. C. Ashoori, and P. Jarillo-Herrero, Nature **556**, 80 (2018).
- [4] M. Yankowitz, S. Chen, H. Polshyn, Y. Zhang, K. Watanabe, T. Taniguchi, D. Graf, A. F. Young, and C. R. Dean, Science **363**, 1059 (2019).
- [5] X. Lu, P. Stepanov, W. Yang, M. Xie, M. A. Aamir, I. Das, C. Urgell, K. Watanabe, T. Taniguchi, G. Zhang, A. Bachtold, A. H. MacDonald, and D. K. Efetov, Nature **574**, 653 (2019).
- [6] X. Liu, Z. Hao, E. Khalaf, J. Y. Lee, Y. Ronen, H. Yoo, D. Haei Najafabadi, K. Watanabe, T. Taniguchi, A. Vishwanath, and P. Kim, Nature **583**, 221 (2020).
- [7] G. W. Burg, J. Zhu, T. Taniguchi, K. Watanabe, A. H. MacDonald, and E. Tutuc, Phys. Rev. Lett. **123**, 197702 (2019).

- [8] C. Shen, Y. Chu, Q. Wu, N. Li, S. Wang, Y. Zhao, J. Tang, J. Liu, J. Tian, K. Watanabe, T. Taniguchi, R. Yang, Z. Y. Meng, D. Shi, O. V. Yazyev, and G. Zhang, *Nat. Phys.* **16**, 520 (2020).
- [9] Y. Cao, D. Rodan-Legrain, O. Rubies-Bigorda, J. M. Park, K. Watanabe, T. Taniguchi, and P. Jarillo-Herrero, *Nature* **583**, 215 (2020).
- [10] G. Chen, L. Jiang, S. Wu, B. Lyu, H. Li, B. L. Chittari, K. Watanabe, T. Taniguchi, Z. Shi, J. Jung, Y. Zhang, and F. Wang, *Nat. Phys.* **15**, 237 (2019).
- [11] G. Chen, A. L. Sharpe, P. Gallagher, I. T. Rosen, E. J. Fox, L. Jiang, B. Lyu, H. Li, K. Watanabe, T. Taniguchi, J. Jung, Z. Shi, D. Goldhaber-Gordon, Y. Zhang, and F. Wang, *Nature* **572**, 215 (2019).
- [12] J. M. Park, Y. Cao, K. Watanabe, T. Taniguchi, and P. Jarillo-Herrero, *Nature* **590**, 249 (2021).
- [13] Z. Hao, A. M. Zimmerman, P. Ledwith, E. Khalaf, D. H. Najafabadi, K. Watanabe, T. Taniguchi, A. Vishwanath, and P. Kim, *Science* **371**, 1133 (2021).
- [14] Y. Cao, J. M. Park, K. Watanabe, T. Taniguchi, and P. Jarillo-Herrero, *Nature* **595**, 526 (2021).
- [15] H. Kim, Y. Choi, C. Lewandowski, A. Thomson, Y. Zhang, R. Polski, K. Watanabe, T. Taniguchi, J. Alicea, and S. Nadj-Perge, *Nature* **606**, 494 (2022).
- [16] Y. Zeng, Z. Xia, K. Kang, J. Zhu, P. Knüppel, C. Vaswani, K. Watanabe, T. Taniguchi, K. F. Mak, and J. Shan, *Nature* **622**, 69 (2023).
- [17] J. Cai, E. Anderson, C. Wang, X. Zhang, X. Liu, W. Holtzmann, Y. Zhang, F. Fan, T. Taniguchi, K. Watanabe, Y. Ran, T. Cao, L. Fu, D. Xiao, W. Yao, and X. Xu, *Nature* **622**, 63 (2023).
- [18] F. Xu, Z. Sun, T. Jia, C. Liu, C. Xu, C. Li, Y. Gu, K. Watanabe, T. Taniguchi, B. Tong, J. Jia, Z. Shi, S. Jiang, Y. Zhang, X. Liu, and T. Li, *Phys. Rev. X* **13**, 031037 (2023).
- [19] Z. Lu, T. Han, Y. Yao, A. P. Reddy, J. Yang, J. Seo, K. Watanabe, T. Taniguchi, L. Fu, and L. Ju, *Nature* **626**, 759 (2024).
- [20] N. R. Chebrolu, B. L. Chittari, and J. Jung, *Phys. Rev. B* **99**, 235417 (2019).
- [21] M. Koshino, *Phys. Rev. B* **99**, 235406 (2019).
- [22] Y.-H. Zhang, D. Mao, Y. Cao, P. Jarillo-Herrero, and T. Senthil, *Phys. Rev. B* **99**, 075127 (2019).
- [23] J. Liu, Z. Ma, J. Gao, and X. Dai, *Phys. Rev. X* **9**, 031021 (2019).
- [24] B. L. Chittari, G. Chen, Y. Zhang, F. Wang, and J. Jung, *Phys. Rev. Lett.* **122**, 016401 (2019).
- [25] J. Y. Lee, E. Khalaf, S. Liu, X. Liu, Z. Hao, P. Kim, and A. Vishwanath, *Nat. Commun.* **10**, 5333 (2019).
- [26] M. König, S. Wiedmann, C. Brüne, A. Roth, H. Buhmann, L. W. Molenkamp, X.-L. Qi, and S.-C. Zhang, *Science* **318**, 766 (2007).
- [27] C.-Z. Chang, J. Zhang, X. Feng, J. Shen, Z. Zhang, M. Guo, K. Li, Y. Ou, P. Wei, L.-L. Wang, Z.-Q. Ji, Y. Feng, S. Ji, X. Chen, J. Jia, X. Dai, Z. Fang, S.-C. Zhang, K. He, Y. Wang, L. Lu, X.-C. Ma, and Q.-K. Xue, *Science* **340**, 167 (2013).
- [28] Y. Xia, D. Qian, D. Hsieh, L. Wray, A. Pal, H. Lin, A. Bansil, D. Grauer, Y. S. Hor, R. J. Cava, and M. Z. Hasan, *Nat. Phys.* **5**, 398 (2009).
- [29] Y. L. Chen, J. G. Analytis, J.-H. Chu, Z. K. Liu, S.-K. Mo, X. L. Qi, H. J. Zhang, D. H. Lu, X. Dai, Z. Fang, S. C. Zhang, I. R. Fisher, Z. Hussain, and Z.-X. Shen, *Science* **325**, 178 (2009).
- [30] T. Zhang, P. Cheng, X. Chen, J.-F. Jia, X. Ma, K. He, L. Wang, H. Zhang, X. Dai, Z. Fang, X. Xie, and Q.-K. Xue, *Phys. Rev. Lett.* **103**, 266803 (2009).
- [31] A. L. Sharpe, E. J. Fox, A. W. Barnard, J. Finney, K. Watanabe, T. Taniguchi, M. A. Kastner, and D. Goldhaber-Gordon, *Science* **365**, 605 (2019).
- [32] M. Serlin, C. L. Tschirhart, H. Polshyn, Y. Zhang, J. Zhu, K. Watanabe, T. Taniguchi, L. Balents, and A. F. Young, *Science* **367**, 900 (2020).
- [33] G. Chen, A. L. Sharpe, E. J. Fox, Y.-H. Zhang, S. Wang, L. Jiang, B. Lyu, H. Li, K. Watanabe, T. Taniguchi, Z. Shi, T. Senthil, D. Goldhaber-Gordon, Y. Zhang, and F. Wang, *Nature* **579**, 56 (2020).
- [34] Y. Wang, J. Herzog-Arbeitman, G. W. Burg, J. Zhu, K. Watanabe, T. Taniguchi, A. H. MacDonald, B. A. Bernevig, and E. Tutuc, *Nat. Phys.* **18**, 48 (2022).
- [35] B. Lian, F. Xie, and B. A. Bernevig, *Phys. Rev. B* **102**, 041402 (2020).
- [36] Q. Wu, J. Liu, Y. Guan, and O. V. Yazyev, *Phys. Rev. Lett.* **126**, 056401 (2021).
- [37] J. A. Crosse, N. Nakatsuji, M. Koshino, and P. Moon, *Phys. Rev. B* **102**, 035421 (2020).
- [38] B. Lian, F. Xie, and B. A. Bernevig, *Phys. Rev. B* **103**, L161405 (2021).
- [39] J. Herzog-Arbeitman, Z.-D. Song, N. Regnault, and B. A. Bernevig, *Phys. Rev. Lett.* **125**, 236804 (2020).
- [40] M. He, Y. Li, J. Cai, Y. Liu, K. Watanabe, T. Taniguchi, X. Xu, and M. Yankowitz, *Nat. Phys.* **17**, 26 (2021).
- [41] See Supplemental Material [url] which includes refs. [42-45], for additional information about the experimental methods and theoretical calculations.
- [42] C. R. Dean, A. F. Young, I. Meric, C. Lee, L. Wang, S. Sorgenfrei, K. Watanabe, T. Taniguchi, P. Kim, K. L. Shepard, and J. Hone, *Nat. Nanotechnol.* **5**, 722 (2010).
- [43] R. Ribeiro-Palau, S. Chen, Y. Zeng, K. Watanabe, T. Taniguchi, J. Hone, and C. R. Dean, *Nano Lett.* **19**, 2583 (2019).
- [44] A. C. Ferrari, J. C. Meyer, V. Scardaci, C. Casiraghi, M. Lazzeri, F. Mauri, S. Piscanec, D. Jiang, K. S. Novoselov, S. Roth, and A. K. Geim, *Phys. Rev. Lett.* **97**, 187401 (2006).
- [45] B. A. Bernevig, T. L. Hughes, and S.-C. Zhang, *Science* **314**, 1757 (2006).
- [46] P. Streda, *Journal of Physics C: Solid State Physics* **15**, L1299 (1982).
- [47] R. Bistritzer and A. H. MacDonald, *Physical Review B* **84**, 035440 (2011).
- [48] J. Yu, B. A. Foutty, Z. Han, M. E. Barber, Y. Schattner, K. Watanabe, T. Taniguchi, P. Phillips, Z.-X. Shen, S. A. Kivelson, and B. E. Feldman, *Nat. Phys.* **18**, 825 (2022).
- [49] K. P. Nuckolls, M. Oh, D. Wong, B. Lian, K. Watanabe, T. Taniguchi, B. A. Bernevig, and A. Yazdani, *Nature* **588**, 610 (2020).
- [50] Y. Saito, J. Ge, L. Rademaker, K. Watanabe, T. Taniguchi, D. A. Abanin, and A. F. Young, *Nat. Phys.* **17**, 478 (2021).
- [51] Y. Xie, A. T. Pierce, J. M. Park, D. E. Parker, E. Khalaf, P. Ledwith, Y. Cao, S. H. Lee, S. Chen, P. R. Forrester, K. Watanabe, T. Taniguchi, A. Vishwanath, P. Jarillo-Herrero, and A. Yacoby, *Nature* **600**, 439 (2021).

Supplemental Material: Emergent Symmetry and Valley Chern Insulator in Twisted Double-Bilayer Graphene

Yimeng Wang, G. William Burg, Biao Lian, Takashi Taniguchi, Kenji Watanabe,
B. Andrei Bernevig, Emanuel Tutuc

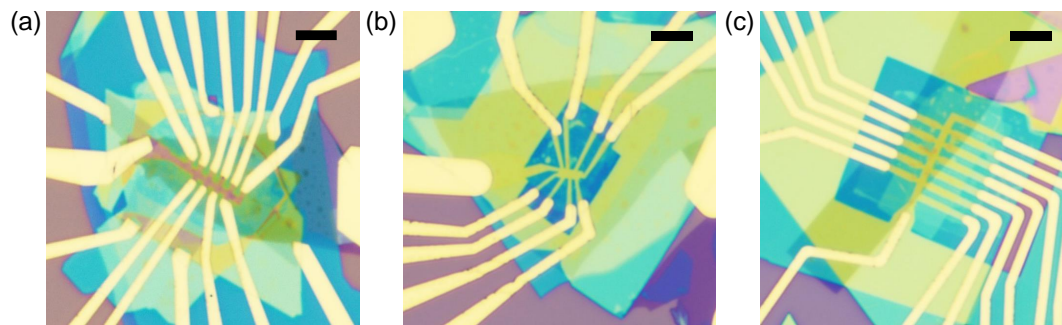


Figure S1: Optical micrographs of the (a) $\theta = 0.97^\circ$, (b) $\theta = 1.01^\circ$, and (c) $\theta = 1.33^\circ$ TDBG device. Device in (a) has a graphene bottom gate and added substrate gate for thermodynamic measurements. Device in (b) and (c) are used for activation measurements. The scale bars are $5 \mu\text{m}$.

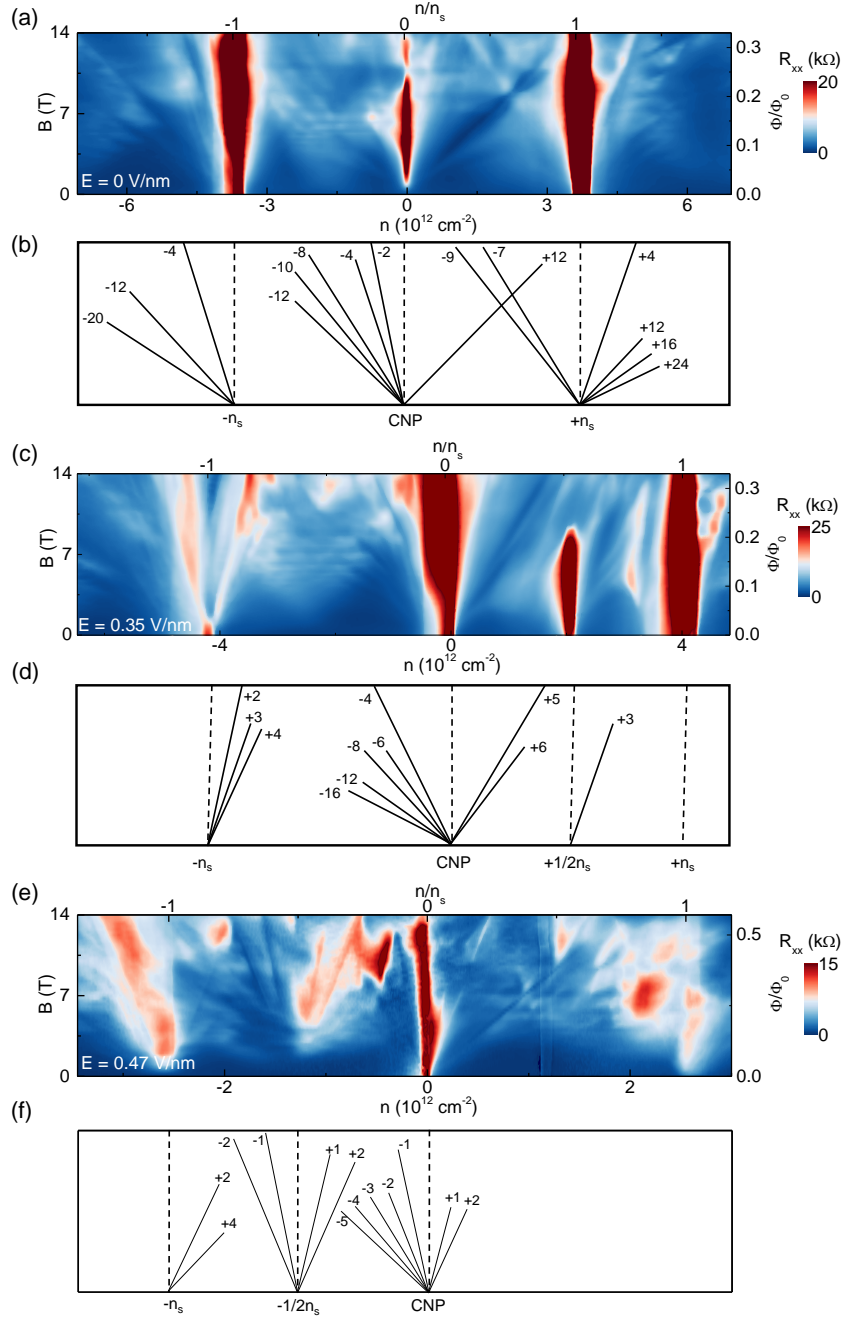


Figure S2: (a, c) R_{xx} vs. n and B in the $\theta = 1.33^\circ$ TDBG sample at (a) $E = 0 \text{ V/nm}$ and (c) $E = 0.35 \text{ V/nm}$, and (e) the $\theta = 1.01^\circ$ TDBG sample at $E = 0.47 \text{ V/nm}$. The top x-axes show n/n_s and the right y-axes show Φ/Φ_0 . (b, d, f) Quantum Hall states observed in panel (a), (c) and (e), respectively, labeled with their corresponding ν values. R_{xx} vs. n and B data for the $\theta = 0.97^\circ$ sample can be found in Ref. [S1].

I Methods

Sample Fabrication

All constituent 2D materials in the twisted double bilayer graphene (TDBG) devices - graphene, hBN, and graphite - are mechanically exfoliated. Graphite gates and hBN dielectrics have both been shown to improve carrier mobility in graphene compared to metal gates and thin film oxide dielectrics [S2, S3]. Large area bilayer graphene are identified by optical contrast on SiO₂/Si substrate, and the layer thickness is confirmed with Raman spectroscopy and fitting of the 2D band of the Raman spectrum [S4]. hBN flakes with smooth surface and uniform thickness are chosen based on their optical contrast on SiO₂/Si substrate and atomic force microscopy. Typically, a thickness of 20-40 nm is chosen for all hBN dielectrics. A bilayer graphene flake is patterned into two separate mesas using electron beam lithography and O₂ plasma etching, which will form the top and bottom bilayers of the TDBG. The heterostructure is then assembled through a series of dry transfers which uses PDMS/PPC hemispherical stamps to selectively pick up and stack the desired layers. Few-layer graphite are used to contact the thin graphene bottom gate [S1]. A target twist angle of $\sim 1.3^\circ$ is used during transfers, and the layers typically relax towards 0° by $\sim 0.1 - 0.3^\circ$ during the process. To improve layer adhesion and reduce bubbles, the 2D flakes and stacks are annealed for one hour at 250 – 310°C at various stages throughout the fabrication. CHF₃ and O₂ plasma etching is used to create the Hall-bar shape and expose the one-dimensional edges of the TDBG, followed by electron beam evaporation of Cr/Pd/Au edge contacts.

Measurement Setup

The four-point resistance of the TDBG channel is measured using low frequency lock-in amplifier techniques, with an excitation current of 1-10 nA. For thermodynamic measurements, the frequency of the source current in the TDBG layer and the bottom gate layer are set to be

different to avoid crosstalk. The channel density (n) and the electric field (E) are controlled by the bias voltage on each gate. As a function of the top (V_{TG}) and bottom (V_{BG}) gate biases, n and E are given by $n = (V_{\text{TG}}C_{\text{TG}} + V_{\text{BG}}C_{\text{BG}})/e$, $E = (V_{\text{TG}}C_{\text{TG}} - V_{\text{BG}}C_{\text{BG}})/2\epsilon_0$, where C_{TG} and C_{BG} are the top and bottom gate capacitances per unit area, e is the electron charge, and ϵ_0 is the vacuum permittivity. The charge neutrality activation gap is determined by fitting the linear portion of the temperature dependence of the log-scale resistance (Fig. 2e inset) to the Arrhenius equation $R_{\text{xx}} \propto e^{-\Delta/2kT}$, where k is the Boltzmann constant.

II Transverse Electric Field vs On-site Energy Difference

While experimental data is measured as a function of the applied transverse electric field E controlled by the top and bottom gates, calculations are done in terms of the on-site energy difference (V) between adjacent graphene layers. In the absence of screening, V is related to E by $V = eEd$, where e is the electron charge and d is the inter-layer spacing. Screening will however reduce V with respect to eEd . In order to evaluate the screening effect in TDBG, we studied a TDBG with a larger twist angle $\theta = 2.61^\circ$. By comparing the R_{xx} vs. n/n_s and E (Fig. S3a) with the calculated density of states (DOS) (Fig. S3b), we extract the linear relation $V/(eE) = 0.027$ nm.

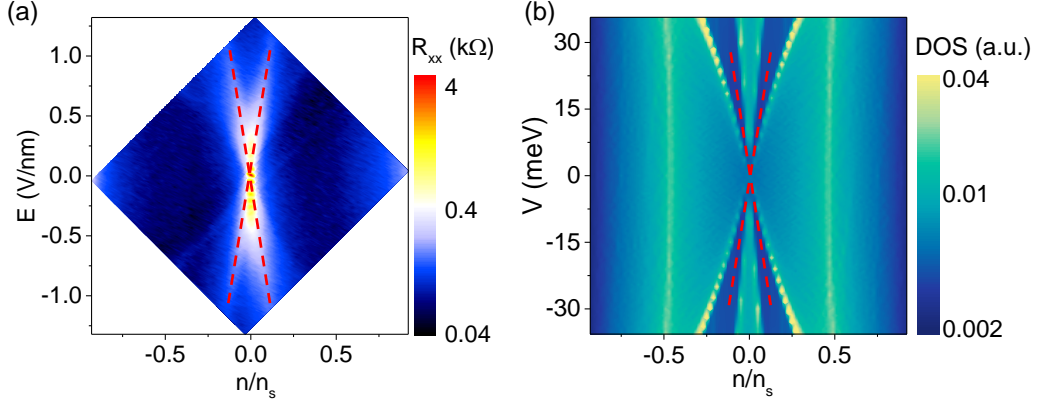


Figure S3: (a) R_{xx} vs. n/n_s and E measured in a TDBG sample with $\theta = 2.61^\circ$ at $T = 1.5$ K. (b) DOS vs. n/n_s and V calculated for $\theta = 2.61^\circ$ TDBG. Red dashed lines mark the resistance maxima in (a) and DOS minima in (b).

III Continuum model for TDBG

We use the continuum model of the TDBG constructed analogous to the Bistritzer-Macdonald model [S5] to calculate the TDBG band structure and Hofstadter butterfly. In real space, the TDBG model (which has no spin-orbit coupling) with AB-AB stacking (A,B for two graphene sublattices) at valley η ($\eta = \pm 1$ for valleys K and K' , respectively) we use is given by [S6–S10]

$$H^{(\eta)}(\mathbf{r}) = \begin{pmatrix} h_{\theta/2}^\eta(-i\nabla) + \frac{3V}{2} & T_{AB} & 0 & 0 \\ T_{AB}^\dagger & h_{\theta/2}^\eta(-i\nabla) + \frac{V}{2} & T^\eta(\mathbf{r}) & 0 \\ 0 & T^\eta(\mathbf{r})^\dagger & h_{-\theta/2}^\eta(-i\nabla) - \frac{V}{2} & T_{AB} \\ 0 & 0 & T_{AB}^\dagger & h_{-\theta/2}^\eta(-i\nabla) - \frac{3V}{2} \end{pmatrix}, \quad (1)$$

where the basis is sorted in the order of 4 graphene layers, each of which has a sublattice basis A and B. The upper two layers form AB stacking, so do the lower two layers, and there is a relative twist angle θ between them. $h_{\pm\theta/2}^\eta$ is the Dirac Hamiltonian of each layer twisted by $\pm\theta/2$, and is given by

$$h_{\pm\theta/2}^\eta(-i\nabla) = \hbar v \begin{pmatrix} & e^{\pm i\eta\theta/2}(i\eta\partial_x - \partial_y) \\ e^{\mp i\eta\theta/2}(i\eta\partial_x + \partial_y) & \end{pmatrix}, \quad (2)$$

where the basis is graphene sublattices A and B, $\hbar v \approx 610\text{meV}\cdot\text{nm}$ is the Fermi velocity of monolayer graphene. The hopping matrices are given by

$$T_{AB} = 3w \begin{pmatrix} 0 & 0 \\ 1 & 0 \end{pmatrix}, \quad T^\eta(\mathbf{r}) = w \sum_{j=1}^3 T_j^\eta e^{i\eta\mathbf{q}_j\cdot\mathbf{r}}, \quad T_j^\eta = \begin{pmatrix} u_0 & e^{i\frac{2\pi\eta(j-1)}{3}} \\ e^{-i\frac{2\pi\eta(j-1)}{3}} & u_0 \end{pmatrix}, \quad (3)$$

where $w = 110\text{ meV}$, and $0 \leq u_0 \leq 1$ is the relaxation parameter. Lastly, V is the displacement field (potential energy) in z direction. The vectors $\mathbf{q}_j = k_m(\sin(2(j-1)\pi/3), -\cos(2(j-1)\pi/3))$, where $k_m = 8\pi \sin(\theta/2)/3a$, with $a = 0.246\text{ nm}$ being the graphene lattice constant. By Fourier transforming the Hamiltonian $H^{(\eta)}(\mathbf{r})$ in Eq. (1) into the momentum space as $H^{(\eta)}(\mathbf{k})$ and taking a momentum space reciprocal lattice ultraviolet cutoff, we can calculate the band structure of TDBG.

We note that here we only keep the nearest neighbor hoppings between layers. Further neighbor hoppings may modify the details of the band structure, but do not qualitatively affect the band topology. In addition, each band is spin \uparrow, \downarrow degenerate. We also note that we are not using an effective model with quadratic Dirac band at valley K or K' in each AB bilayer and a moiré potential between them. This is because this would lead to inaccuracies in the band dispersions, and would make it inconvenient to add the interlayer potential V between each neighboring pair of the 4 layers.

When calculating the band structure in Fig. 1d-e, we have used the zero angle approximation, namely, approximating θ to zero in the Dirac Hamiltonian $h_{\pm\theta/2}^\eta(-i\nabla)$, which leads to a particle-hole symmetric band structure (see Eq. (4) and the discussion below it). In addition, we use a relaxation parameter $u_0 = 0.9$, which is typical for twist angle θ near 1° [S7, S8]. Larger energy range of the band structure with zero angle approximation is shown in Fig. S4, where one can identify the single-particle gaps at $n = \pm 3n_s$ observed in our experiment. The band structure without zero-angle approximation is shown in Fig. S5 and discussed at the end of this section. The difference between band structures with and without zero angle approximation is

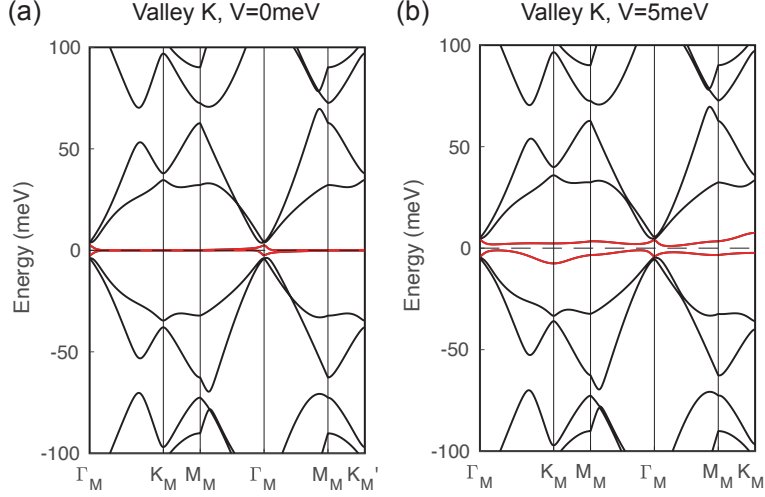


Figure S4: Larger energy range of the TDBG band structure calculated with the zero-angle approximation at valley K , angle $\theta = 1.01^\circ$, relaxation parameter $u_0 = 0.9$ and for interlayer potential $V = 0$ meV and $V = 5$ meV.

negligibly small.

Under the zero angle approximation, at zero interlayer potential $V = 0$, the lowest two bands of each valley are gapless at K_M and K'_M of the Moiré Brillouin zone (MBZ). In this case, the TDBG has time-reversal symmetry T , C_{3z} symmetry, and C_{2x} symmetry. Here all the symmetries are defined as spinless, namely, they do not act on electron spin. Besides, the zero angle approximation yields an anti-unitary particle-hole (PH) symmetry P defined (in real space) by

$$P = C_{2z}T \otimes \delta_{\eta\eta'} \begin{pmatrix} & & I_2 \\ & -I_2 & \\ -I_2 & I_2 & \end{pmatrix}, \quad (4)$$

which satisfies $PH^{(\eta)}(\mathbf{r})P^{-1} = -H^{(\eta)}(-\mathbf{r})$ for the real space Hamiltonian $H^{(\eta)}(\mathbf{r})$ in Eq. (1). In Eq. (4), I_2 is the 2×2 identity matrix, and the 8×8 matrix share the same basis as the Hamiltonian in Eq. (1). This symmetry operation can be rewritten in the momentum space (by

Fourier transformation) as

$$PH^{(\eta)}(\mathbf{k})P^{-1} = -H^{(\eta)}(-\mathbf{k}), \quad (5)$$

where the origin of \mathbf{k} is at Γ_M point of the moiré BZ. We note that there is no C_{2z} symmetry because of the AB stacking of each bilayer. Therefore, without $C_{2z}T$ symmetry, the fragile topology in TBG protected by $C_{2z}T$ is absent here in TDBG. On the other hand, the quadratic band touchings at K_M and K'_M points are protected by the $C_{2x}P$ symmetry and C_{3z} symmetry. This is because the combined operation $C_{2x}P$ and the rotation C_{3z} satisfies

$$(C_{2x}P)H^{(\eta)}(\mathbf{k})(C_{2x}P)^{-1} = -H^{(\eta)}(-C_{2x}\mathbf{k}), \quad C_{3z}H^{(\eta)}(\mathbf{k})C_{3z}^{-1} = H^{(\eta)}(C_{3z}\mathbf{k}), \quad (6)$$

and the commutation relation

$$(C_{2x}P)C_{3z}(C_{2x}P)^{-1} = C_{3z}^{-1}, \quad (7)$$

where we have used $C_{2x}C_{3z}C_{2x}^{-1} = C_{3z}^{-1}$ and $PC_{3z}P^{-1} = C_{3z}$. Since K_M and K'_M points are invariant under C_{3z} and $C_{2x}P$ (as $\mathbf{k} = -C_{2x}\mathbf{k} = C_{3z}\mathbf{k}$ when \mathbf{k} is at K_M or K'_M), the energy eigenstates at K_M or K'_M fall into irreducible representations of C_{3z} and $C_{2x}P$. In particular, Eqs. (6) and (7) and the fact that $C_{2x}P$ is anti-unitary allows eigenstates at K_M (K'_M) occupying a one-dimensional representation of C_{3z} and $C_{2x}P$ pinned at zero energy with a fixed C_{3z} eigenvalue. For instance, for a zero-energy C_{3z} eigenstate $|\frac{2\pi}{3}, K_M\rangle$ satisfying $C_{3z}|\frac{2\pi}{3}, K_M\rangle = e^{2\pi i/3}|\frac{2\pi}{3}, K_M\rangle$, we have $C_{3z}(C_{2x}P|\frac{2\pi}{3}, K_M\rangle) = C_{2x}PC_{3z}^{-1}|\frac{2\pi}{3}, K_M\rangle = C_{2x}P(e^{-2\pi i/3}|\frac{2\pi}{3}, K_M\rangle) = e^{2\pi i/3}C_{2x}P|\frac{2\pi}{3}, K_M\rangle$, which allows one to have a state $|\frac{2\pi}{3}, K_M\rangle = C_{2x}P|\frac{2\pi}{3}, K_M\rangle$ forming a one-dimensional representation. Its energy is pinned at zero because $C_{2x}P$ flips the energy (Eq. (6)). In TDBG, the two states at K_M (K'_M) of each valley and spin occupy two zero-energy one-dimensional representations with C_{3z} eigenvalues $e^{\pm 2\pi i/3}$, respectively, thus are degenerate.

Further, we briefly explain here why K_M (K'_M) has quadratic band touching in our TDBG model. There is generically no symmetry forbidding the quadratic band touching to split into 1

linear Dirac cone at K_M (K'_M) and 3 surrounding linear Dirac cones (along the three $K_M M_M$ ($K'_M M_M$) directions) satisfying the C_{3z} symmetry and $C_{2x}P$ symmetry. Here we have quadratic band touching because our model (Eq. (1)) has only kept the nearest interlayer hopping between B atom of the first layer and A atom of the second layer (which sit on top of each other) in the upper (lower) Bernal stacking bilayer graphene (BLG). To understand this, we take the K_M point at valley K as an example. Exactly at K_M point, the momentum coincide with K point of the original graphene valley of the upper Bernal stacking BLG, so we can use the C_{3z} eigenvalues of the upper BLG basis to figure out the C_{3z} eigenvalues of TDBG states. Since the 4 basis of the upper BLG ($1A, 1B, 2A, 2B$, standing for A, B sublattices of layers 1 and 2) have C_{3z} eigenvalues ($e^{2\pi i/3}, 1, 1, e^{-2\pi i/3}$), respectively, the TDBG zero-energy eigenstate with C_{3z} eigenvalue $e^{2\pi i/3}$ ($e^{-2\pi i/3}$) should have its wave function in the upper BLG subspace only nonzero on the basis $1A$ ($2B$). In fact, the $e^{2\pi i/3}$ eigenstate has a wave function nonzero on basis $1A$ and exactly zero on all the other basis of the upper and lower BLG, as one can easily verify. When the momentum deviates from K_M point, since there is no direct hopping between basis $1A$ and $2B$, the lowest perturbation away from zero energy is second order, which is quadratic in k . This is similar to the situation in a single Bernal stacking BLG.

At nonzero interlayer potential V , the C_{2x} symmetry is broken, and the lowest two bands are gapped. The charge neutrality gap at valley η ($\eta = \pm 1$ for valleys K and K') and interlayer potential V carries a Chern number $C_\eta = 2\eta \text{sgn}(V)$, where $\text{sgn}(x)$ is the sign function. In realistic samples, the interlayer potential V is proportional to the externally applied transverse electric field E in our experiment. In the absence of charge screening, one would have $V = eEd$, where e is the electron charge, and $d = 0.6708\text{nm}$ is the interlayer distance between neighboring graphene layers. In reality, however, the electrons in the TDBG will screen the external electric field and reduce the interlayer potential. See Sec.II of this supplemental material for the ratio between E and V .

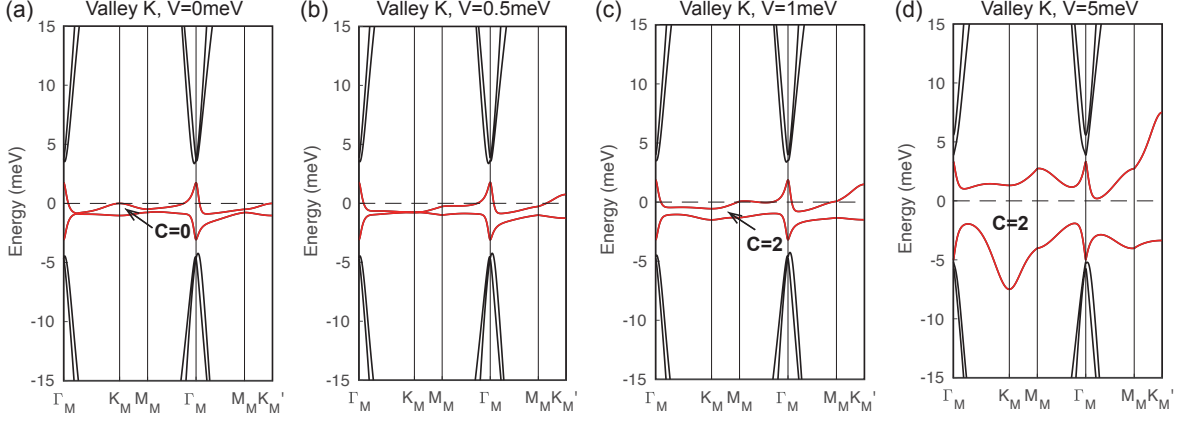


Figure S5: The TDBG band structure calculated without the zero-angle approximation at valley K , angle $\theta = 1.01^\circ$, relaxation parameter $u_0 = 0.9$ and various interlayer potential V . The band structure at valley K' is related to that at K by time-reversal symmetry. The interlayer potential V is set as (a) $V = 0$ meV, (b) $V = 0.5$ meV, (c) $V = 1$ meV, and (d) $V = 5$ meV.

In comparison, we have plotted the $\theta = 1.01^\circ$ TDBG band structure (at valley K) without the zero angle approximation in Fig. S5, which does not have the particle-hole symmetry P . Accordingly, the quadratic band touchings at K_M and K'_M are no longer protected at interlayer potential $V = 0$, but opens a small Chern number $C = 0$ direct charge-neutrality gap at $V = 0$ (Fig. S5a). For $\theta = 1.01^\circ$, there is still no indirect gap at $V = 0$ (Fig. S5a). As the interlayer potential V increases to $V \approx 0.5$ meV, the band structure undergoes a gap closing transition at K_M (K'_M) in valley K (K'), after which (i.e., $V > 0.5$ meV) the charge-neutrality gap becomes a Chern number $C_K = 2$ ($C_{K'} = -2$) gap (Fig. S5b-d). (The case with $V < 0$ is related to the case with $V > 0$ by C_{2x} .) Therefore, without zero angle approximation, the valley Chern number $C_V = (C_K - C_{K'})/2 = 2\text{sgn}(V)$ holds for $|V| > 0.5$ meV. Since an interlayer potential 0.5 meV is quite small and can hardly be experimentally resolved (corresponding to electric field $E \sim 0.01$ V/nm), the conclusion without zero angle approximation is not very different from that with zero angle approximation.

The Hofstadter spectra for the TDBG continuum model in Fig. 3d-e are calculated using the

momentum space method in Refs. [S11,S12], with the zero-angle approximation used.

IV The closing of Chern gap at nonzero magnetic flux

Here we prove that a 2D system with a Chern number C gap between a conduction band of Chern number $-C$ and a valence band of Chern number C is forced to close at magnetic flux $\Phi/\Phi_0 = 1/|C|$.

We define the electron filling density (total number of electrons per unit area) in the Chern number C gap as n_C . Since the system only has two bands at zero magnetic field, the number of electrons per unit cell has to be between 0 and 2, thus we have a physical bound

$$0 \leq n_C \leq \frac{2}{A}, \quad (8)$$

where A is the zero-magnetic-field unit cell area. At zero magnetic flux, the filling, for a chemical potential in the Chern gap, is $n_C = 1/A$.

At nonzero magnetic field, n_C in the Chern gap - defined by adiabatic continuity to zero field, is determined by the Streda formula as

$$n_C = \frac{1}{A} \left(1 + C \frac{\Phi}{\Phi_0} \right). \quad (9)$$

For $\Phi/\Phi_0 > 1/|C|$, we would have the filling of the Chern gap $n_C < 0$ or $n_C > 2/A$ if the Chern gap persists, in contradiction with the physical bound of n_C . Therefore, the Chern number C gap must close at or before $\Phi/\Phi_0 = 1/|C|$.

V Non-closure of gap between trivial bands

Generically, if the bands above (and below) a band gap are topologically trivial, the band gap will remain open in nonzero magnetic fields, and will usually increase with respect to magnetic field B at small B . This is because a well-behaved trivial band usually have Landau levels

(LLs) from the band bottom (top) moving upwards (downwards) as a function of B because of the positive (negative) effective electron Newtonian mass at the band bottom (top), leading to a narrowing of the bandwidth. Accordingly, no LL disperses into the band gap above or below the trivial band. The LLs from top and bottom of the same band generically annihilate with each other around the van Hove singularity in the middle of the band, leading to a Hofstadter butterfly bounded by the bandwidth of the trivial band [S11, S13].

We note that if a trivial band has a complicated enough dispersion (e.g., because the hopping range is longer than usual), it could have its bandwidth increased at nonzero magnetic field B , and thus the band gap above or below it could narrow down at nonzero B . However, this would generically not close the band gap between two trivial bands, since nothing forbids opening the gap between the two trivial bands at any magnetic field B (unless fine tuned) [S11, S13]. Generically, for trivial gapped bands, one can always increase the Hamiltonian gap beyond the value of the increased band-width due to the application of B , which would result in a full gap at all values of B .

In contrast, a topological band can have LLs protected to disperse into the band gap above or below the band. For instance, the 2-band tight-binding model in Eq. (11) in the Chern insulator phase can be expanded into a $k \cdot p$ model at small \mathbf{k} as

$$H_{k,p}(\mathbf{k}) = [-m_0 + m_1(k_x^2 + k_y^2)]\sigma_z + k_x\sigma_x - k_y\sigma_y, \quad (10)$$

where $m_0 > 0$ and $m_1 > 0$ (for Eq. (11), $m_0 = 2 - M$ and $m_1 = 1/2$). Note that $m_0 m_1 > 0$ is the band-inversion condition for the two bands to be Chern bands [S14]. This gives rise to a zero-mode LL with energy $-m_0 + m_1 eB/\hbar$, which emerges from the lower Chern band and disperses linearly into the gap, and finally leads to the closing of the Chern band gap at large B . This is the continuum description of our band-closing phenomenon.

VI Tight-binding models for Fig. 3a-c

Here we give the tight-binding models we use for calculating the Hofstadter butterflies in Fig. 3a-c.

Fig. 3a-b is calculated by a 2D tight-binding model with a momentum space Hamiltonian

$$H_{\text{TB1}}(\mathbf{k}) = (M - \cos k_x - \cos k_y)\sigma_z + \sigma_x \sin k_x - \sigma_y \sin k_y, \quad (11)$$

where $\sigma_{x,y,z}$ are the Pauli matrices in the 2-band basis. We note that this model is half of the Bernevig-Hughes-Zhang model [S14]. The valence band and conduction band of this model have Chern numbers 0 if $|M| > 2$, while have Chern numbers $\pm \text{sgn}(M)$ respectively when $|M| < 2$. Fig. 3a is calculated at $M = 3$, and Fig. 3b is calculated at $M = 1$.

Fig. 3c is calculated by a 2D tight-binding model with a momentum space Hamiltonian

$$H_{\text{TB2}}(\mathbf{k}) = (M - \cos k_x - \cos k_y)\sigma_z + \sigma_x(\cos k_x - \cos k_y) + \sigma_y[\cos(k_x - k_y) - \cos(k_x + k_y)]. \quad (12)$$

The valence band and conduction band of this model have Chern numbers 0 if $|M| > 2$, while have Chern numbers $\pm 2\text{sgn}(M)$ respectively when $|M| < 2$. Fig. 3c is calculated at $M = 1$.

VII Mean field theory for the interaction effect

Here we propose a simplified toy model for the TDBG under magnetic field, and give a mean field theory understanding for the interaction effect in Fig. 4. This mean field theory will be further verified in Supplemental Material (SM) Sec. VIII by Hartree-Fock numerical calculations for an interacting tight-binding model.

Under an interlayer potential $V > 0$, the charge neutrality gap at valley η ($\eta = \pm 1$ for valleys K and K', respectively) has Chern number $C_\eta = 2\eta$. Accordingly, the first valence band and first conduction band of valley η carry Chern numbers C_η and $-C_\eta$, respectively. At zero magnetic field, we assume the energies of the first conduction band range within $M_1 \leq \epsilon_{+, \eta, s} \leq$

M_0 , and the energies of the first valence band range within $-M_0 \leq \epsilon_{-, \eta, s} \leq -M_1$, where $M_0 > M_1 > 0$ (see Fig. 4b). We shall ignore all the higher bands.

Under a magnetic flux Φ , the two flat bands develop into Hofstadter spectra. For model simplification, we define all the single-particle Hofstadter subbands emerging from the conduction band as the "conduction states", and define those emerging from the valence band as the "valence states". In other words, for each graphene valley, the conduction states and valence states are identified as those states above and below the Chern gap (emerging from the charge neutrality), respectively. According to our Hofstadter butterfly calculation (Fig. 3d-e), the energies of the conduction/valence states under nonzero magnetic flux Φ are different for different valleys. A good approximation to the single-particle energy ranges of the conduction states and valence states is (for $\Phi/\Phi_0 \leq 0.5$)

$$\epsilon_{+, \eta, s}(\Phi) \in [\Delta_{+, \eta}(\Phi), M_0] , \quad \epsilon_{-, \eta, s}(\Phi) \in [-M_0, \Delta_{-, \eta}(\Phi)] ,$$

$$\Delta_{m, \eta}(\Phi) = mM_1 \left(1 - \frac{2\Phi}{\Phi_0} \right) + \eta M_0 \frac{2\Phi}{\Phi_0} , \quad (13)$$

where $\epsilon_{+, \eta, s}(\Phi)$ and $\epsilon_{-, \eta, s}(\Phi)$ are the energies of conduction and valence states, respectively, $\eta = \pm 1$ is the valley index, and $s = \pm 1$ for spin up and down. We note that at small B field, the linear dispersions of band energy ranges in Eq. (13) can also be justified by the Landau level calculations for the $\mathbf{k} \cdot \mathbf{p}$ Hamiltonian of 2-band Chern insulator models (e.g., the tight-binding models in Eqs. (11) and (12), see also the $\mathbf{k} \cdot \mathbf{p}$ model in Eq. (10)), which yields zero mode LLs linear dispersing from the positive Chern number band towards the negative Chern number band. But we also note that $\mathbf{k} \cdot \mathbf{p}$ models do not have a finite bandwidth; so our interpolation formula in Eq. (13) is based on the small B field behavior of the $\mathbf{k} \cdot \mathbf{p}$ model and the fact that the gap between the two bands, as well as the bandwidth of the Chern number -2 band, both vanishes at $\Phi/\Phi_0 = 0.5$ (at which all electron states of the Chern number -2 band are transferred into the Chern number $+2$ band). The Zeeman splitting energy (~ 1 meV

at $\Phi/\Phi_0 = 0.5$) is small and thus ignored here. For each particular η and s , the gap between conduction and valence states closes at $\Phi/\Phi_0 = 0.5$ at energy ηM_0 , and the bandwidth of the Chern number -2 band also vanishes at $\Phi/\Phi_0 = 0.5$ due to the Streda formula. With all spins and valleys, the (non-interacting) gap between conduction and valence states closes at $\Phi/\Phi_0 = \frac{M_1}{2(M_0+M_1)} < 0.5$ due to energy overlaps among different spins and valleys, as illustrated by Fig. 4b.

On the other hand, the average number of conduction/valence electron states per area at valley η , spin s is given by the Streda formula as (for $\Phi/\Phi_0 \leq 0.5$)

$$N_{m,\eta}(\Phi) = \frac{1}{A_M} \left(1 - mC_\eta \frac{\Phi}{\Phi_0} \right) = \frac{1}{A_M} \left(1 - 2m\eta \frac{\Phi}{\Phi_0} \right), \quad (14)$$

which is independent of s , where $m = \pm$ for conduction and valence states, respectively, and A_M is the Moiré unit cell area. To simplify the model, we assume these $N_{m,\eta}(\Phi)$ states are evenly distributed in the energy range of $\epsilon_{m,\eta,s}(\Phi)$ given in Eq. (13), namely, the density of states is uniform within the bandwidth of each $\{m, \eta, s\}$ given in Eq. (13).

The system thus contains 8 species of electron states, labeled by $\{m, \eta, s\}$ with $m = \pm$, $\eta = \pm 1$, and $s = \uparrow, \downarrow$. These electron states, which are spread uniformly in the energy range of Eq. (13), can be either occupied by electrons or not, and the average number of occupied electrons per area $n_{m,\eta,s}$ of species $\{m, \eta, s\}$ has to satisfy

$$0 \leq n_{m,\eta,s} \leq N_{m,\eta}(\Phi). \quad (15)$$

Since we assumed the density of states of each electron species $\{m, \eta, s\}$ is uniform in the energy range given by Eq. (13), here we can assume the electron density $n_{m,\eta,s}$ uniformly occupy the lowest $n_{m,\eta,s}/N_{m,\eta}(\Phi)$ fraction of the energy range of species $\{m, \eta, s\}$ in Eq. (13). The corresponding kinetic energy per area of the electrons of species $\{m, \eta, s\}$ can then be derived to be

$$E_{+, \eta, s}^0(\Phi, n_{+, \eta, s}) = \int_0^{n_{+, \eta, s}} \epsilon_{+, \eta, s}(\Phi, n) dn = \Delta_{+, \eta}(\Phi) n_{+, \eta, s} + \frac{M_0 - \Delta_{+, \eta}(\Phi)}{2N_{+, \eta}(\Phi)} n_{+, \eta, s}^2,$$

$$E_{-, \eta, s}^0(\Phi, n_{-, \eta, s}) = \int_0^{n_{-, \eta, s}} \epsilon_{-, \eta, s}(\Phi, n) dn = -M_0 n_{-, \eta, s} + \frac{M_0 + \Delta_{-, \eta}(\Phi)}{2N_{-, \eta}(\Phi)} n_{-, \eta, s}^2, \quad (16)$$

where we have defined

$$\epsilon_{+, \eta, s}(\Phi, n) = \Delta_{+, \eta}(\Phi) + \frac{n}{D_{+, \eta, s}(\Phi)}, \quad \epsilon_{-, \eta, s}(\Phi, n) = -M_0 + \frac{n}{D_{-, \eta, s}(\Phi)}$$

as the electron single-particle energy at density n above the band bottom of species $\{m, \eta, s\}$, and $D_{+, \eta, s}(\Phi) = N_{+, \eta}(\Phi)/(M_0 - \Delta_{+, \eta}(\Phi))$ and $D_{-, \eta, s}(\Phi) = N_{-, \eta}(\Phi)/(\Delta_{-, \eta}(\Phi) + M_0)$ are the density of states of electron species $\{+, \eta, s\}$ and $\{-, \eta, s\}$, respectively (which we assumed are energy independent).

We then assume there is a short-range repulsive interaction $U_0 \geq 0$ between two electrons of different species when their distance is within the size of the Moiré unit cell area A_M . Two electrons within the same species $\{m, \eta, s\}$ do not overlap with each other due to the Pauli exclusion principle, thus they approximately do not interact with each other (in other words, gain an exchange energy). This leads to a mean-field interaction energy per area (for $\Phi/\Phi_0 \leq 1/2$):

$$\mathcal{H}_I(\Phi, n_{m, \eta, s}) = \frac{U_0 A_M}{2} \sum_{m, m', \eta, \eta', s, s'} \gamma_{m\eta s}^{m'\eta' s'}(\Phi) \left(n_{m, \eta, s} - \frac{N_{m, \eta}(\Phi)}{2} \right) \left(n_{m', \eta', s'} - \frac{N_{m', \eta'}(\Phi)}{2} \right) \quad (17)$$

where we have defined the factor

$$\gamma_{m\eta s}^{m'\eta' s'}(\Phi) = 1 - \delta_{m, m'} \delta_{\eta, \eta'} \delta_{s, s'} - \delta_{m, -m'} \delta_{\eta, \eta'} \delta_{s, s'} \zeta(\Phi), \quad (18)$$

with $\zeta(\Phi)$ being some function almost zero for $\Phi/\Phi_0 < 1/2$ not close to $1/2$, but quickly grows to 1 when Φ/Φ_0 approaches $1/2$ (e.g, $\zeta(\Phi) = (2\Phi/\Phi_0)^\alpha$ with a large α). The choice of factor $\gamma_{m\eta s}^{m'\eta' s'}(\Phi)$ in Eq. (18) accounts for two assumptions: first, two electrons within the same species $\{m, \eta, s\}$ approximately have zero interaction with each other due to Pauli exclusion. Second, the interaction between an electron in band $\{+, \eta, s\}$ and an electron in band $\{-, \eta, s\}$

is generically U_0 when Φ/Φ_0 is not close to $1/2$, since they have distinct orbital wave functions; but since the single-particle bands $\{+, \eta, s\}$ and $\{-, \eta, s\}$ merge together and begin to have similar orbital wave functions at $\Phi/\Phi_0 = 1/2$, the interaction between them should tend to zero (hence $\zeta(\Phi)$ tends to 1) at $\Phi/\Phi_0 = 1/2$ due to the Pauli exclusion principle according to our assumption. Besides, in defining the interaction in Eq. (17), we subtract each density $n_{m,\eta,s}$ by a half-filling fraction $N_{m,\eta}(\Phi)/2$ of the band $\{m, \eta, s\}$, so that the interaction preserves the many-body particle-hole symmetry (the single-particle PT symmetry followed by an interchange of electron creation and annihilation operators) of TDBG about the charge neutrality in magnetic fields, which maps $n_{m,\eta,s}$ to $N_{-m,-\eta}(\Phi) - n_{-m,-\eta,s}$.

Up to a constant, the interaction energy per area in Eq. (17) can be rewritten as

$$\mathcal{H}_I(\Phi, n_{m,\eta,s}) = \frac{U_0 A_M}{2} \left\{ n_{\text{tot}}^2 - \frac{8n_{\text{tot}}}{A_M} + \sum_{\{m,\eta,s\}} \left[N_{m,\eta}(\Phi) n_{m,\eta,s} - n_{m,\eta,s}^2 - \zeta(\Phi) (n_{m,\eta,s} n_{-m,\eta,s} - n_{m,\eta,s} N_{-m,\eta}(\Phi)) \right] \right\}, \quad (19)$$

where $n_{\text{tot}} = \sum_{m,\eta,s} n_{m,\eta,s}$ is the total number of electrons, and we have used the fact that $\sum_{m,\eta,s} N_{m,\eta}(\Phi) = 8/A_M$.

This leads to a mean field total energy per area:

$$\mathcal{H}(\Phi, n_{m,\eta,s}) = \sum_{m,\eta,s} E_{m,\eta,s}^0(\Phi, n_{m,\eta,s}) + \mathcal{H}_I(\Phi, n_{m,\eta,s}). \quad (20)$$

At charge neutrality, the electron filling is restricted to be the total filling of the four flat valence bands:

$$n_{\text{tot}} = \sum_{m,\eta,s} n_{m,\eta,s} = 4/A_M. \quad (21)$$

At zero magnetic flux $\Phi = 0$, the mean field total energy per area takes a simple form (up to a constant)

$$\mathcal{H}(0, n_{m,\eta,s}) = \sum_{\eta,s} (M_1 n_{+, \eta, s} - M_0 n_{-, \eta, s}) - \frac{(M_0 - M_1 + U_0) A_M}{2} \sum_{m,\eta,s} n_{m,\eta,s}^2, \quad (22)$$

where $0 \leq n_{m,\eta,s} \leq 1/A_M$. Under the restriction of Eq. (21), the first term linear in $n_{m,\eta,s}$ favors as many valence states ($m = -1$) being occupied as possible, while the second term quadratic in $n_{m,\eta,s}$ favors as many species $\{m, \eta, s\}$ being maximally occupied as possible. Therefore, the ground state is easily found to have $n_{+,\eta,s} = 0$ and $n_{-,\eta,s} = 1/A_M$ for every η and s , namely, all the conduction states are empty, and all the valence states are occupied.

We want to examine whether such a state with all conduction states empty and all valence states occupied,

$$n_{+,\eta,s} = 0, \quad n_{-,\eta,s} = N_{-,\eta}(\Phi), \quad (23)$$

is still the ground state at nonzero magnetic flux Φ . We therefore expand the energy functional to linear order deviation from Eq. (23) subject to condition (21), which gives an energy variation:

$$\delta\mathcal{H}(\Phi, \delta n_{m,\eta,s}) = \sum_{m,\eta,s} \left[\Delta_{m,\eta}(\Phi) + m \frac{U_0 A_M}{2} (N_{m,\eta}(\Phi) - \zeta(\Phi) N_{-m,\eta}(\Phi)) \right] \delta n_{m,\eta,s}, \quad (24)$$

where

$$\delta n_{+,\eta,s} = n_{+,\eta,s} \geq 0, \quad \delta n_{-,\eta,s} = n_{-,\eta,s} - N_{-,\eta}(\Phi) \leq 0 \quad (25)$$

are the density deviations from the state in Eq. (23), and $\sum_{m,\eta,s} \delta n_{m,\eta,s} = 0$.

The interaction energy variation for moving $\delta n = \sum_{\eta,s} \delta n_{+,\eta,s} = -\sum_{\eta,s} \delta n_{-,\eta,s}$ number of electrons per area from the valence states ($m = -1$) to the conduction states ($m = +1$) (note that $\sum_{\eta,s} \delta n_{+,\eta,s}$ is opposite to $\sum_{\eta,s} \delta n_{-,\eta,s}$ so that the total number of electrons is kept constant) satisfies

$$\delta\mathcal{H}(\Phi, \delta n_{m,\eta,s}) \geq \Delta(\Phi) \delta n, \quad (26)$$

where

$$\begin{aligned} \Delta(\Phi) &= \min_{\eta=\pm 1} \left[\Delta_{+,\eta}(\Phi) + \frac{U_0 A_M}{2} (N_{+,\eta}(\Phi) - \zeta(\Phi) N_{-,\eta}(\Phi)) \right] \\ &\quad - \max_{\eta=\pm 1} \left[\Delta_{-,\eta}(\Phi) - \frac{U_0 A_M}{2} (N_{-,\eta}(\Phi) - \zeta(\Phi) N_{+,\eta}(\Phi)) \right] \\ &= 2M_1 \left(1 - \frac{2\Phi}{\Phi_0}\right) + U_0(1 - \zeta(\Phi)) - |2M_0 - U_0(1 + \zeta(\Phi))| \frac{2\Phi}{\Phi_0}. \end{aligned} \quad (27)$$

Eq. (26) shows that if $\Delta(\Phi) \geq 0$, the state in Eq. (23) would be the ground state, and $\Delta(\Phi)$ would be the electron gap of the system at charge neutrality. For concreteness, we take the function $\zeta(\Phi)$ defined in Eq. (18) (for $\Phi/\Phi_0 \leq 1/2$) as a function which is approximately zero for $\Phi/\Phi_0 < \frac{1}{2} - \delta$, and only considerably nonzero within the interval $\frac{1}{2} - \delta \leq \Phi/\Phi_0 \leq \frac{1}{2}$, where $\delta \ll 1$ (e.g., a broken-line function $\zeta(\Phi) = \Theta(\Phi/\Phi_0 - 1/2 + \delta)[1 - \delta^{-1}(1/2 - \Phi/\Phi_0)]$ with $\Theta(x)$ being the Heaviside step function). We then find that:

(1) if the interaction strength $0 < U_0 < M_0$, the charge neutrality gap $\Delta(\Phi)$ will close at $\Phi/\Phi_0 = \frac{2M_1 + U_0}{4M_0 + 4M_1 - 2U_0} < \frac{1}{2}$;

(2) if the interaction strength $U_0 \geq M_0$, the charge neutrality gap $\Delta(\Phi)$ will close at some flux within the range $\frac{1}{2} - \delta < \Phi/\Phi_0 \leq \frac{1}{2}$, namely, in the vicinity of $\frac{1}{2}$ flux per unit cell. In particular, the gap closes exactly at $\Phi/\Phi_0 = \frac{1}{2}$ when $U_0 = M_0$ which is independent of the form of the function $\zeta(\Phi)$. The closer U_0 and M_0 are to each other, the closer the gap closing is to flux $\Phi/\Phi_0 = 1/2$. In the realistic TDBG systems, the interaction U_0 from Coulomb potential can be estimated to be about $10 \sim 20$ meV (using the moiré lattice constant) for $\theta \approx 1^\circ$ and dielectric constant $5 \sim 10$ (the substrate hBN has dielectric constant ~ 6). In comparison, the single-particle bandwidths M_0 in main text Fig. 1 are around 5 to 10 meV. Therefore, one expects $U_0 > M_0$ but not significantly larger, so the gap closing point is expected to be close to $\Phi/\Phi_0 = 0.5$. This provides an explanation to our experiment where the valley Chern gap closing happens around $\Phi/\Phi_0 = 0.5$.

Heuristically, this is because moving an electron from the fully filled valence states of all spins and valleys to an empty conduction state costs interaction energy, thus the charge neutrality gap tends to be stabilized by the interaction. For a given electron species (band) $\{m, \eta, s\}$, the interaction Eq. (17) yields a mean-field chemical potential

$$\mu_{m,\eta,s}(\Phi) = \frac{U_0 A_M}{2} \sum_{m',\eta',s'} \gamma_{m\eta s}^{m'\eta's'}(\Phi) \langle n_{m',\eta',s'} - \frac{N_{m',\eta'}(\Phi)}{2} \rangle. \quad (28)$$

For the density configuration of fully occupied valence bands in Eq (23), the effective chemical potential of band $\{m, \eta, s\}$ reads

$$\begin{aligned}\mu_{m,\eta,s}(\Phi) &= m \frac{U_0 A_M}{2} (N_{m,\eta}(\Phi) - \zeta(\Phi) N_{-m,\eta}(\Phi)) \\ &= \frac{U_0}{2} [m(1 - \zeta(\Phi)) - 2\eta(1 + \zeta(\Phi)) \frac{\Phi}{\Phi_0}].\end{aligned}\tag{29}$$

This leads to a deformation of band energies as shown in Fig. 4d, where the gap between conduction and valence bands at each valley η is generically enlarged and shifted towards zero energy for $0 \leq \Phi/\Phi_0 < 1/2$. Note that the function $\zeta(\Phi)$ reaching 1 at $\Phi/\Phi_0 = 1/2$ (which we assumed) is necessary here for the Chern gap of each valley to close at $\Phi/\Phi_0 = 1/2$, which is the requirement of band topology (as long as the emergent valley U(1) symmetry is unbroken). As a result, the two Chern gaps of the two valleys tend to align with each other and keep the charge neutrality gap open. For $U_0 \geq M_0$, the two Chern gaps are sufficiently enlarged and shifted towards each other, so that the net charge neutrality gap remains open for $\Phi/\Phi_0 < \frac{1}{2} - \delta \approx \frac{1}{2}$.

Lastly, we add a few more comments on the factor $\gamma_{m\eta s}^{m'\eta's'}(\Phi)$ and the function $\zeta(\Phi)$ in Eq. (18). We have used a simplified interaction which is zero for two electrons within the same band $\{m, \eta, s\}$. Besides, at $\Phi/\Phi_0 = 1/2$, the interaction between bands $\{+, \eta, s\}$ and $\{-, \eta, s\}$ also becomes zero. In practice, two electrons within the same band gain an exchange energy from the Pauli exclusion principle, making the interaction between them, which we denote as U'_0 , smaller than that between different bands (U_0), namely, $U'_0 < U_0$. In general, U'_0 is not exactly zero. Accordingly, one also requires the interaction between bands $\{+, \eta, s\}$ and $\{-, \eta, s\}$ to reach U'_0 at $\Phi/\Phi_0 = 1/2$, since at $\Phi/\Phi_0 = 1/2$ the two bands $\{+, \eta, s\}$ and $\{-, \eta, s\}$ merge into one (due to band topology), and should gain the same exchange energy as that within each band. Such an interaction is equivalent to the interaction in Eq. (17) with U_0 replaced by $U_0 - U'_0$, plus a term $U'_0 A_M n_{\text{tot}}^2 / 2 - 4U'_0 n_{\text{tot}}$ which is a constant when the total number of electrons $n_{\text{tot}} = \sum_{m,\eta,s} n_{m,\eta,s}$ is fixed. The function $\zeta(\Phi) = 1$ at $\Phi/\Phi_0 = 1/2$ is still required by the merging of the two bands $\{+, \eta, s\}$ and $\{-, \eta, s\}$ at $\Phi/\Phi_0 = 1/2$. But

for $\Phi/\Phi_0 < 1/2$ not too close to $1/2$ where the orbital wave functions of bands $\{+, \eta, s\}$ and $\{-, \eta, s\}$ are sufficiently different, the exchange energy gain between $\{+, \eta, s\}$ and $\{-, \eta, s\}$ should be small, and thus $\zeta(\Phi)$ should remain small. Therefore, all our conclusions in the above still hold, except that U_0 is replaced by $U_0 - U'_0$.

VIII Hartree-Fock numerical calculation of the Hofstadter spectrum

To verify our mean field theory in SM Sec. VII, we perform a Hartree-Fock calculation for the following tight-binding toy model with on-site interaction:

$$\begin{aligned}
H &= H_0 + H_I, \\
H_0 &= \sum_{\eta=\pm 1, s=\uparrow, \downarrow} \sum_{j_x, j_y} M c_{j_x, j_y, \eta, s}^\dagger \sigma_z c_{j_x, j_y, \eta, s} + \left[c_{j_x, j_y, \eta, s}^\dagger \left(\frac{\sigma_x - \sigma_z}{2} \right) c_{j_x+1, j_y, \eta, s} \right. \\
&\quad \left. - c_{j_x, j_y, \eta, s}^\dagger \left(\frac{\sigma_x + \sigma_z}{2} \right) c_{j_x, j_y+1, \eta, s} + \eta c_{j_x, j_y, \eta, s}^\dagger \frac{\sigma_y}{2} c_{j_x+1, j_y+1, \eta, s} - \eta c_{j_x, j_y, \eta, s}^\dagger \frac{\sigma_y}{2} c_{j_x+1, j_y-1, \eta, s} + h.c. \right], \\
H_I &= U \sum_{j_x, j_y, \eta, s, \alpha} \left(c_{j_x, j_y, \eta, s, \alpha}^\dagger c_{j_x, j_y, \eta, s, \alpha} - \frac{1}{2} \right)^2,
\end{aligned} \tag{30}$$

where (j_x, j_y) labels the coordinate of lattice sites, $\eta = \pm 1$ is the valley index, $s = \uparrow, \downarrow$ is spin, $\alpha = +, -$ is the orbital index, and $c_{j_x, j_y, \eta, s} = (c_{j_x, j_y, \eta, s, +}, c_{j_x, j_y, \eta, s, -})^T$ denotes the electron annihilation operator. $\sigma_{x,y,z}$ are the pauli matrices in the orbital α basis. The free Hamiltonian H_0 is simply the tight-binding model in Eq. (12) ($\eta = +1, s = \uparrow, \downarrow$) plus its time-reversal transformation ($\eta = -1, s = \uparrow, \downarrow$). We set $M = 1$ (as we did in the main text Fig. 3c), in which case the free Hamiltonian H_0 has a valley Chern number $C_\eta = 2\eta$ at half filling (charge neutrality).

We then add a magnetic flux per original unit cell $\Phi/\Phi_0 = p/q$, where p and q are integers (the lattice constants in x and y directions are set to 1). We take the Landau gauge $\mathbf{A} = (0, \frac{2\pi p}{q} x)$, and adopt the standard Peierls substitution that the hopping t_{ji} from site \mathbf{R}_i to \mathbf{R}_j

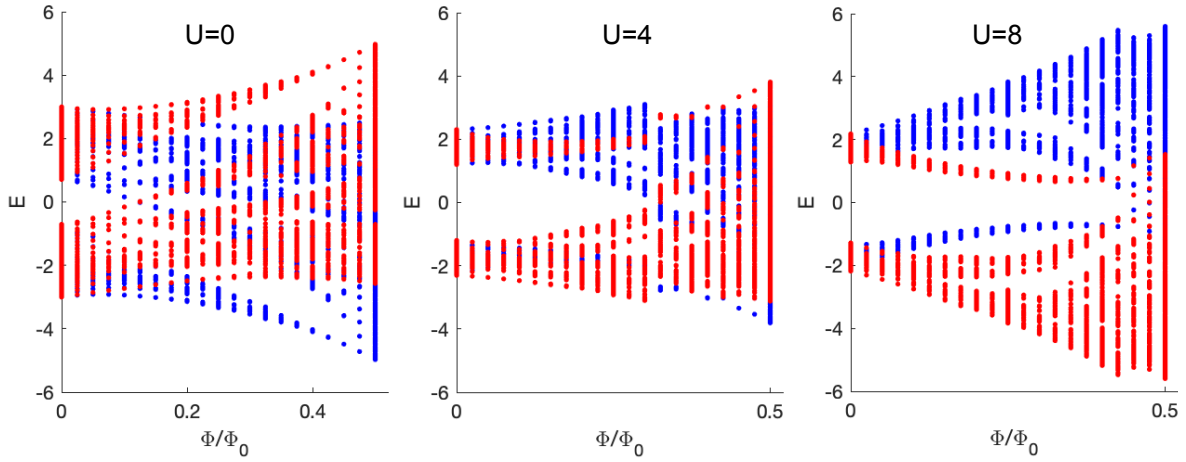


Figure S6: Hartree-Fock numerical calculation for the Hofstadter butterfly of the tight-binding toy model with valley Chern number 2 in Eq. (30). Here the magnetic flux $\Phi/\Phi_0 = p/q$, where we set $q = 40$, and $0 \leq p \leq 20$ is an integer. U is the on-site Hubbard interaction. Red and blue stand for the spectra in valleys $\eta = +$ and $\eta = -$, respectively.

changes into $t_{ji} e^{i \int_{\mathbf{R}_i}^{\mathbf{R}_j} \mathbf{A} \cdot d\mathbf{r}}$, where the integral in the exponent is along the straight line segment from \mathbf{R}_i to \mathbf{R}_j . If p and q are already coprime, the free Hamiltonian H_0 then has a magnetic unit cell of size $q \times 1$.

To do the Hartree-Fock calculation, we fix the electron filling at $n = 4$ electrons per original (zero magnetic field) unit cell. We assume there is no translational symmetry breaking or valley symmetry breaking. The standard Hartree and Fock terms are then given by

$$\begin{aligned}
 H_{HF} &= \sum_{\eta, s, \alpha} \sum_{j_x, j_y} h_{j_x, j_y, \eta, s, \alpha}^{HF} c_{j_x, j_y, \eta, s, \alpha}^\dagger c_{j_x, j_y, \eta, s, \alpha} \\
 h_{j_x, j_y, \eta, s, \alpha}^{HF} &= \sum_{\{\eta', s'\} \neq \{\eta, s\}} \left(\langle c_{j_x, j_y, \eta, s, \alpha}^\dagger c_{j_x, j_y, \eta', s', \alpha} \rangle - \frac{1}{2} \right).
 \end{aligned} \tag{31}$$

The expectation value $\langle c_{j_x, j_y, \eta, s, \alpha}^\dagger c_{j_x, j_y, \eta', s', \alpha} \rangle$ in Eq. (31) can be calculated iteratively from the mean field ground state, which can be obtained by diagonalizing the mean field Hamiltonian $H_0 + H_{HF}$ and filling the energy levels up to the desired number of electrons ($n = 4$ electrons per original unit cell). By doing such iterations until convergence, we can obtain the Hartree-

Fock spectrum at magnetic flux $\Phi/\Phi_0 = p/q$.

In numerical calculations, we set $q = 40$, and $0 \leq p \leq 20$ (then reduce p and q into coprime pairs). In the magnetic Brillouin zone (which is of size $2\pi/q$ in the k_x direction and 2π in the k_y direction), we discretize the quasimomentum into a momentum lattice of size $(80/q) \times 80$. The resulting Hartree-Fock Hofstadter spectra for interaction strengths $U = 0, 4, 8$ are shown in Fig. S6, where red and blue are the spectra in valleys $\eta = +$ and $\eta = -$, respectively. As we expected from SM Sec. VII, we find the magnetic flux of charge neutrality valley Chern gap closing increases as the interaction U increases. For $U = 8$, the interaction is larger than the free bandwidth, and we see the charge neutrality gap does not close until $\Phi/\Phi_0 = 0.5$.

References

- [S1] Wang, Y. et al. Bulk and edge properties of twisted double bilayer graphene. *Nat. Phys.* **18**, 48 (2022)
- [S2] Dean, C. R. et al. Boron nitride substrates for high-quality graphene electronics. *Nat. Nanotechnol.* **5**, 722 (2010).
- [S3] Ribeiro-Palau, R. et al. High-quality electrostatically defined hall bars in monolayer graphene. *Nano Lett.* **19**, 2583 (2019).
- [S4] Ferrari, A. C. et al. Raman spectrum of graphene and graphene layers. *Phys. Rev. Lett.* **97**, 187401 (2006).
- [S5] Bistritzer, R., MacDonald, A. H. Moiré bands in twisted double-layer graphene. *Proc. Natl. Acad. Sci.* **108**, 12233 (2011).
- [S6] Chebrolu, N. R., Chittari, B. L., Jung, J. Flat bands in twisted double bilayer graphene. *Phys. Rev. B* **99**, 235417 (2019).

- [S7] Koshino, M. Band structure and topological properties of twisted double bilayer graphene. *Phys. Rev. B* **99**, 235406 (2019).
- [S8] Lee, J. L., Khalaf, E., Liu, S., Liu, X., Hao, Z., Kim, P., Vishwanath, A. Theory of correlated insulating behaviour and spin-triplet superconductivity in twisted double bilayer graphene. *Nat. Commun.* **10**, 5333 (2019).
- [S9] Zhang, Y.-H., Mao, D., Cao, Y., Jarillo-Herrero, P., Senthil, T. Nearly flat Chern bands in moiré superlattices. *Phys. Rev. B* **99**, 075127 (2019).
- [S10] Liu, J., Ma, Z., Gao, J., Dai, X. Quantum valley Hall effect, orbital magnetism, and anomalous Hall effect in twisted multilayer graphene systems. *Phys. Rev. X* **9**, 031021 (2019).
- [S11] Lian, B., Xie, F., Bernevig, B. A. Landau level of fragile topology. *Phys. Rev. B* **102**, 041402 (2020).
- [S12] Lian, B., Xie, F., Bernevig, B. A. Open momentum space method for the Hofstadter butterfly and the quantized Lorentz susceptibility. *Phys. Rev. B* **103**, L161405 (2021).
- [S13] Herzog-Arbeitman, J., Song, Z., Regnault, N., Bernevig, B. A. Hofstadter topology: Noncrystalline topological materials at high flux. *Phys. Rev. Lett.* **125**, 236804 (2020).
- [S14] Bernevig, B. A., Hughes, T. L., Zhang, S.-C. Quantum spin Hall effect and topological phase transition in HgTe quantum wells. *Science* **314**, 1757 (2006).